

Research Project Report

**Modelling Pulse Profiles  
of Accreting Neutron Stars:  
Studying the Dependence on  
Geometrical Parameters and the  
Emission Profile**

Lucia Härer

Dr. Karl-Remeis Sternwarte  
Friedrich-Alexander Universität  
Erlangen-Nürnberg

Supervisor: Prof. Dr. Jörn Wilms

September 27, 2021

# Abstract

X-ray emission from accreting neutron stars shows characteristic pulsations, due to the rotation of the neutron star. The pulse profiles can be highly complex, showing asymmetries and multiple peaks. Pulse profiles are shaped by relativistic light bending and the angular dependence of the emission in the investigated energy band. The aim of this project is to model pulse profiles using the relativistic ray-tracing code `LIBANS`, assuming different angular dependences of the emission (emission profiles) for the cap and the wall of the two antipodal accretion columns, considering an energy band far below the cyclotron line energy,  $E < 10$  keV. The choice of emission profiles is motivated by the difference in scattering behaviour of the ordinary and extraordinary photon polarisation modes in the highly magnetised plasma that is present in the accretion region. The accretion column polar angles, the observer inclination, the height of the accretion columns, the relative intensity of cap and wall emission, and polar and azimuthal offsets with respect to the antipodal column configuration are varied and their effects on the pulse profile are discussed. I find a variety of complex pulse profiles, including asymmetric ones for a non-zero offset in the azimuthal column position.

# Contents

<b>Abstract</b>	<b>i</b>
<b>1 Introduction</b>	<b>1</b>
1.1 X-ray pulsars . . . . .	1
1.2 The physics of the accretion region . . . . .	2
1.3 Light bending around neutron stars . . . . .	4
<b>2 Pulse profile modelling</b>	<b>5</b>
2.1 Emission profiles . . . . .	5
2.1.1 $1 + 2 \cos$ profile . . . . .	5
2.1.2 Cap profile after Basko & Sunyaev (1975) . . . . .	7
2.1.3 Inclined Gaussian profile . . . . .	8
2.1.4 Final choice of profiles . . . . .	8
2.2 Additions to the LIBANS code . . . . .	9
<b>3 Results</b>	<b>10</b>
3.1 Simulation setup . . . . .	10
3.2 Comparison of emission profiles . . . . .	11
3.3 Observer inclination . . . . .	14
3.4 Accretion column height . . . . .	15
3.5 Relative intensity of cap and wall emission . . . . .	15
3.6 Asymmetric column configurations . . . . .	15
<b>4 Summary and conclusions</b>	<b>20</b>
<b>Bibliography</b>	<b>21</b>

# 1 Introduction

## 1.1 X-ray pulsars

In the early 1970s, bright, regularly pulsating X-ray sources were discovered (e.g., Giacconi et al. 1971; Tananbaum et al. 1972). These X-ray pulsars were soon suggested to be accreting neutron star systems, in which matter from a companion star is funnelled onto the magnetic poles of the neutron star, where it is rapidly decelerated and its kinetic energy is converted into X-rays (Lamb et al. 1973). The pulsations arise due to an offset between the rotational and the magnetic dipole axis of the neutron star, causing a periodicity in the observed flux.

Two features of neutron stars are decisive for the generation of strong, pulsed X-ray emission: their extraordinary compactness ( $M_{\text{NS}}R_{\text{NS}}^{-1} \sim 1.4 M_{\odot}(10 \text{ km})^{-1}$ , Lattimer 2012) and strong magnetic fields ( $\sim 10^8$ – $10^{14}$  G, see Lai 2001). The compactness allows the accreting matter to gain relativistic velocities by accelerating in the gravitational potential. The kinetic energy is converted into radiation when the matter flow encounters the surface of the neutron star, releasing a power,

$$L = \frac{GM_{\text{NS}}\dot{M}}{R_{\text{NS}}}, \quad (1.1)$$

dependent on the compactness of the neutron star and the mass accretion rate,  $\dot{M}$ . Typical  $\dot{M}$  range from  $10^{15}$ – $10^{17} \text{ g s}^{-1}$ , resulting in an X-ray luminosity  $L_{\text{X}} \sim 10^{35}$ – $10^{37} \text{ erg s}^{-1}$  (see Becker et al. 2012, and references therein).

Due to the strong magnetic field, the accreting matter is forced to follow the field lines inside the Alfvén radius,  $r_{\text{A}}$ , where the energy density of the magnetic field surpasses the kinetic energy density of the accreting matter (Lamb et al. 1973). This channelling effect concentrates the accreting matter at the magnetic poles, in a region that is small compared to the overall surface of the neutron star. The accretion region heats up to  $T \gtrsim 10^8 \text{ K}$  (Basko & Sunyaev 1975) and contains a highly magnetised plasma, the physics of which is discussed in the following section. The effects of the high magnetic field on the plasma are particularly relevant to the study of neutron star high-mass X-ray binaries (NS-HMXBs), which have field strengths  $\gtrsim 10^{12} \text{ G}$ , because these systems are young, due to the short lifetime of the high mass companion, and the field strength decays over time (see Caballero & Wilms 2012).

## 1.2 The physics of the accretion region

The structure of the accretion region on the surface of the neutron star depends on the mass accretion rate,  $\dot{M}$ , and the corresponding X-ray luminosity,  $L_X$ , as indicated in Fig. 1.1. Four regimes can be broadly differentiated, with  $L_X$  increasing from panels a–d (Becker et al. 2012, and references therein):

- (a) At  $L_X \lesssim 10^{34}\text{--}10^{35} \text{ erg s}^{-1}$ , the gas impacts and heats up the surface, forming a hot spot.
- (b) A gas shock develops in the accretion stream.
- (c) A radiative shock forms. However, the radiation field is not strong enough to completely decelerate the matter flow. Instead, the flow dissipates its energy in Coulomb collisions.
- (d) Above a critical X-ray luminosity,  $L_{\text{crit}} \sim 10^{37}\text{--}10^{38} \text{ erg s}^{-1}$ , the radiation field is strong enough to completely decelerate the accretion flow. Emission mainly escapes parallel to the surface.

The integrity of the so-called accretion columns in regimes b–d is maintained by the strong magnetic field. Columns dominated by a radiative shock can reach heights of several kilometres (Becker et al. 2012).

The spectral and angular distribution of the emission emerging from the accretion region is shaped by scattering, absorption, and emission processes in the highly magnetised plasma. At field strengths  $\gtrsim 10^{12} \text{ G}$ , the kinetic energy of electrons perpendicular to the magnetic field lines is quantised into Landau-levels (see Lai 2001). As a result, Compton scattering and free-free absorption show a strong dependence on the angle to the magnetic field,  $\vartheta$ , and the photon energy in the form of resonances at the energies of the Landau levels, also called the cyclotron line energies (e.g., Schwarm et al. 2017; Sokolova-Lapa et al. 2021, and references therein). Spectra of X-ray pulsars can show so-called cyclotron resonant scattering features (CRSFs), broad dips centred at the cyclotron line energies. CRSFs provide a direct means of measuring the magnetic field strength, as it determines the position of the Landau levels (see Lai 2001). For an overview of CRSF detections see Staubert et al. (2019).

A second important aspect of radiative transfer in a highly magnetised environment is that photon-electron interactions depend on photon polarisation (see Sokolova-Lapa et al. 2021, and references therein). Photons whose polarisation vector is in the plane spanned by the magnetic field vector and the photon wave vector are referred to as ordinary photons. The opposite case, where the polarisation vector sticks out of the plane, is called extraordinary. The ordinary mode is typically more anisotropic, while the extraordinary shows strong energy dependence and escapes the accretion column predominately perpendicular to the direction of the magnetic field (e.g., Sokolova-Lapa et al. 2021; Falkner 2018, and references therein).

# 1 Introduction

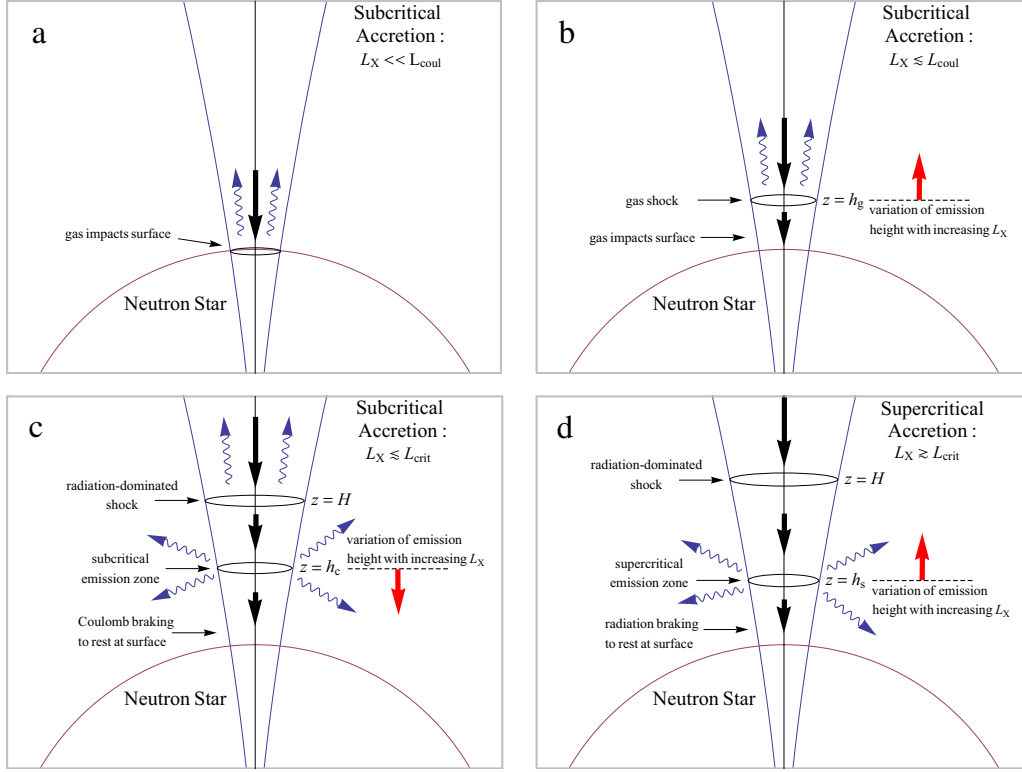


Figure 1.1: Illustration of accretion regimes (Becker et al. 2012, Fig. 1). X-ray luminosity increases consecutively from panels a to d.  $L_{\text{col}}$  and  $L_{\text{crit}}$  refer to the luminosities above which Coulomb collisions and the radiation field, respectively, are sufficient to decelerate the accretion flow to rest. Further description is given in the text.

Modelling these processes self-consistently to predict the spectral, angular, and polarisation dependence of the emerging radiation presents a major challenge. A successful model for the angle-averaged spectrum was presented by Becker & Wolff (2007). Recently, Sokolova-Lapa et al. (2021) introduced a model for the low  $\dot{M}$  regime.

### 1.3 Light bending around neutron stars

General relativity predicts that photon trajectories are bent in strong gravitational fields. This light bending enlarges the visible surface area of accreting X-ray pulsars, because trajectories are curved towards the observer (see Fig. 1.2; Falkner 2012, 2018).

Falkner (2012, 2018) developed the LIBANS (LIght Bending Around Neutron Stars) code to calculate photon trajectories around neutron stars using relativistic ray-tracing, assuming a Schwarzschild metric. The light bending is calculated either numerically according to the exact solution of the Geodesic equation, or assuming the analytic approximation by Beloborodov (2002). Classical trajectories, without light bending effects, can also be calculated. For this project, the exact solution was used. The code allows to adjust various geometric parameters, such as size, height, number, and relative position of accretion columns on the neutron star, allowing for a comparison between different setups. In addition, a function for the angular dependence of the emission (emission profile) and underlying spectral distribution can be chosen.

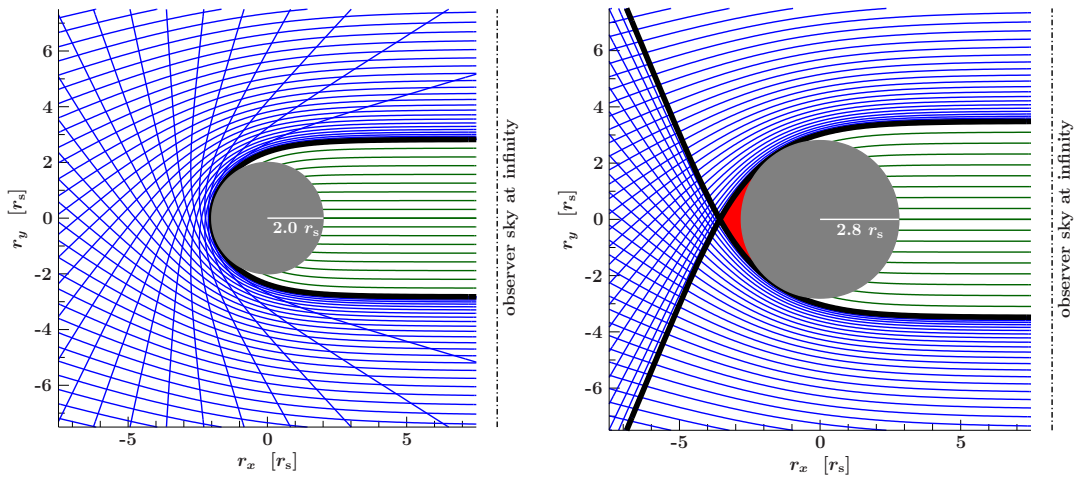


Figure 1.2: Photon trajectories (blue and green) around neutron stars of different radii, given as multiples of their Schwarzschild radius  $r_s$  (Falkner 2012, Fig. 3.9). The red zone indicated in the right panel is in the shadow zone of the neutron star. Photons from this region do not reach the observer.

## 2 Pulse profile modelling

The pulse profile of an accreting neutron star is the dependence of its flux on the rotational phase. Observations of pulse profiles have revealed an astonishing variety of shapes (see Fig. 2.1). Complementary to the spectrum, pulse profiles provide insights in the physics of the accretion region, as they are shaped by the angular dependence of the emission, the so-called emission profile, and light bending (e.g., Falkner 2012, 2018; Härer 2019). Pulse profiles are also strongly impacted by geometric parameters, such as the inclination of the accretion column with respect to the rotational axis,  $\Theta_{AC}$ , and the observer inclination,  $i$  (e.g., Falkner 2012). The large number of free geometrical parameters and the limitations of current physical models make modelling observed pulse profiles a challenge. The aim of this project is to explore a part of this large parameter space with a simple, but not unrealistic setup for the accretion column. In particular, two different emission profiles are chosen for the top and sides of the column (referred to as cap and wall in the following), motivated by the difference in scattering behaviour of the ordinary and extraordinary polarisation modes (see Sect. 1.2). Following a discussion of the emission profiles in Sect. 2.1, additions made to the LIBANS code (Falkner 2012, 2018) will be introduced in Sect. 2.2. The LIBANS was used to set up a geometrical model of the neutron star and calculate the light bending.

### 2.1 Emission profiles

I consider different emission profiles for the accretion column wall and cap, as motivated above. The profiles are appropriate for  $E \sim 1\text{--}10\text{ keV} \ll E_{cyc}$ , where the influence from cyclotron resonant scattering and absorption is minimal.

#### 2.1.1 $1 + 2 \cos$ profile

The wall emission is likely to be dominated by the more isotropic extraordinary mode (see Sect. 1.2), for which the emission profile can be assumed to follow (e.g., Lyubarskii 1986; Postnov et al. 2015; Falkner 2018),

$$I(\gamma) = 1 + 2 \cos \gamma, \quad (2.1)$$

where  $\gamma$  is the angle towards the normal of the column surface. The profile is shown in Fig. 2.2 (dash-dotted green).

## 2 Pulse profile modelling

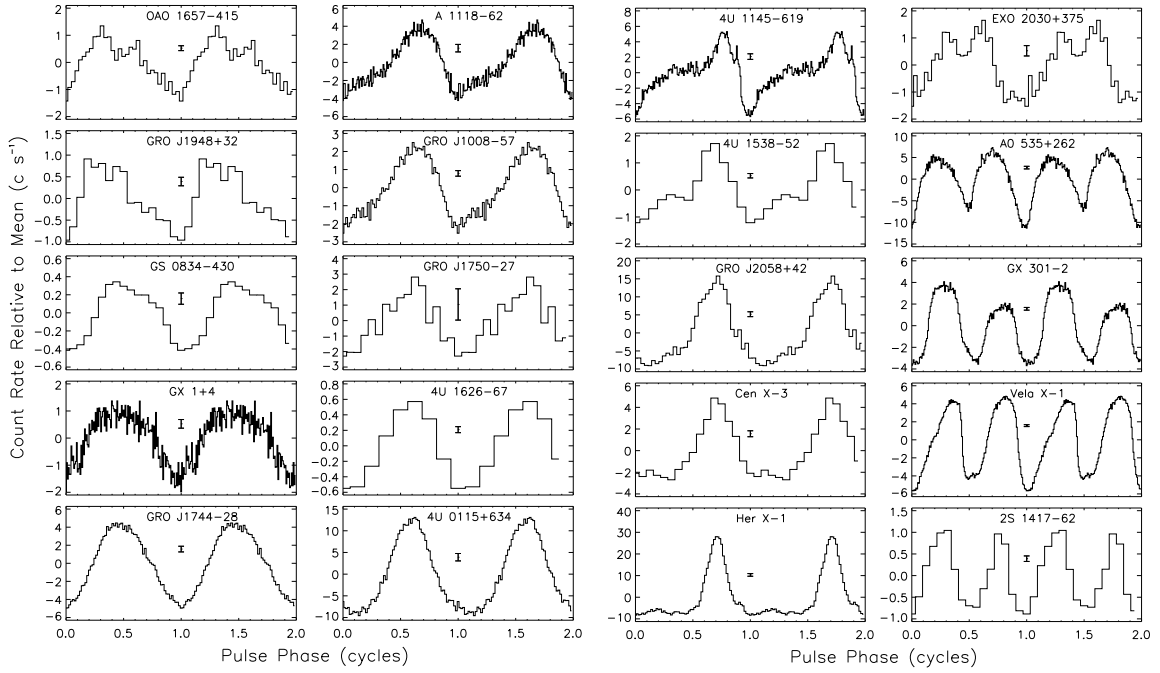


Figure 2.1: Examples of pulse profiles for different accreting neutron stars (Bildsten et al. 1997, Fig. 7). Many of the observed pulse profiles are asymmetric.

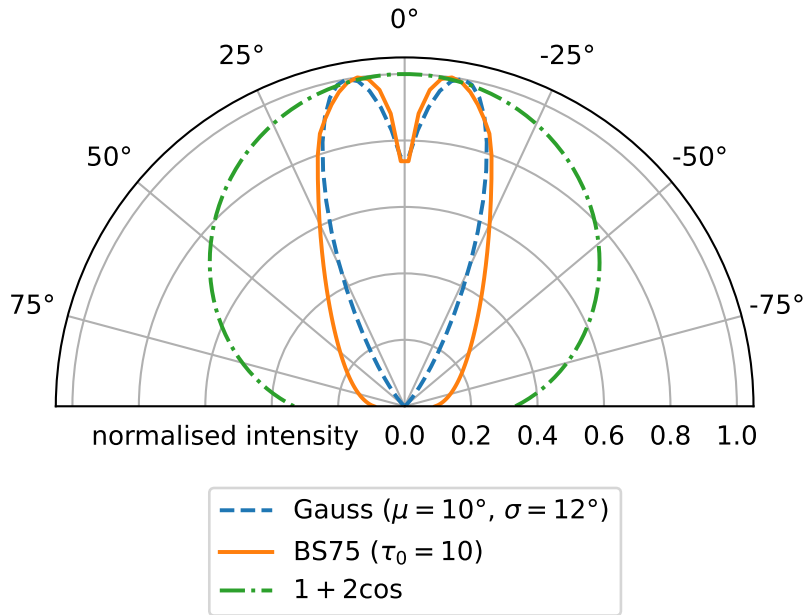


Figure 2.2: Comparison of the different emission profiles: the commonly used  $1 + 2 \cos \vartheta$  profile (dash-dotted green), the profile according to Basko & Sunyaev (1975) (BS75 here; solid orange, Eq. 2.5), and an inclined Gaussian profile, with parameters to match the shape of the BS75 profile (dashed blue, Eq. 2.7).

### 2.1.2 Cap profile after Basko & Sunyaev (1975)

Basko & Sunyaev (1975), BS75 hereafter, obtained an emission profile for  $E \ll E_{\text{cyc}}$  in the hot spot regime, where no gas or radiative shock is present. In this case, the energy of the accretion flow heats up the accretion region by proton-proton collisions and the energy equalises with the plasma electrons by Coulomb interactions. The energy is deposited in the upper layers of the atmosphere following an exponential relation,  $\sim e^{-\tau/\tau_0}$ , where the optical depth of Thomson scattering,  $\tau$ , is used as a measure of the depth of the atmosphere and  $\tau_0 = 20$  corresponds to the mean free path expected for the proton-proton collisions (BS75). BS75 approximate the total Compton scattering cross-sections for  $E \ll E_{\text{cyc}}$  following Canuto et al. (1971),

$$\sigma_{\text{ext}} = \sigma(E/E_{\text{cyc}})^2, \quad (2.2)$$

$$\sigma_{\text{ord}}(\vartheta) = \sigma(\sin^2 \vartheta + (E/E_{\text{cyc}})^2), \quad (2.3)$$

where  $\sigma$  is the cross-section in the non-magnetised case and  $\vartheta$  the angle to the magnetic field. The free-free absorption coefficients are modified by the same coefficients, for the ordinary and extraordinary modes respectively. BS75 argue that generation of radiation in the extraordinary mode and mode conversion can be ignored, as  $E/E_{\text{cyc}}$  is small and ordinary photons are converted into extraordinary photons in deeper layers of the atmosphere at  $\tau > \tau_0$ . BS75 show that the radiative transfer results in a Compton scattering optical depth,

$$\tau_{\text{C}} \sim \sin^2 \vartheta / \cos \vartheta, \quad (2.4)$$

which means that an observer looking onto the hot spot at a small  $\vartheta$  can see deep into the atmosphere, while seeing the top layers of the atmosphere at large  $\vartheta$ . At small  $\vartheta$ , the resulting emission profile is therefore affected by the mode conversion mentioned above, which leads to a dip at  $\vartheta = 0$  (see the orange line in Fig. 2.2). The profile can be expressed as (BS75, Eq. B12)

$$I(\vartheta, \tau_0) \sim \frac{H(\tau_0)H(\cos^2 \vartheta / (1 - \cos^2 \vartheta))}{\cos^2 \vartheta / (1 - \cos^2 \vartheta) + \tau_0}, \quad (2.5)$$

where  $H(x)$  is Chandrasekhar's  $H$ -function.  $H(x)$  is a non-analytical function, therefore the approximations (BS75, Eq. B8; Hapke 2002, Eq. 13),

$$H(x) = \begin{cases} 1.62x / \ln(x)^{0.645} & \text{if } 10 < x \leq 10^4 \\ [1 - x(1 + \frac{1}{2}(1 - 2x) \ln(\frac{1+x}{x}))]^{-1} & \text{if } 0 < x \leq 10 \end{cases} \quad (2.6)$$

are employed here. The emission profile is shown in Fig. 2.3 for several values of  $\tau_0$ . The profile is highly asymmetric, peaking at small  $\vartheta$ . The intensity increases with  $\tau_0$  (Fig. 2.3, left panel) and the profile becomes narrower (right panel). Even though the profile was calculated without considering the effects of a gas shock or a radiative shock, BS75 argue that its basic features should translate to these regimes, because Compton scattering stays the dominant mechanism.

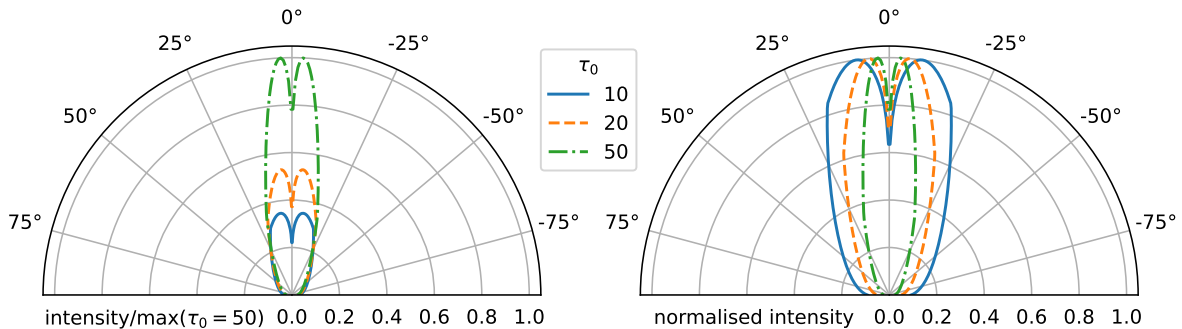


Figure 2.3: Emission profile according to BS75 for different values of  $\tau_0$ . The left panel shows the profiles normalised the maximal intensity of the  $\tau_0 = 50$  profile. In the right panel, the profiles are normalised to their individual maxima to highlight the difference in shape.

### 2.1.3 Inclined Gaussian profile

Iwakiri et al. (2019) fitted pulse profiles from 4U 1626–67 with a model based on the LIBANS code assuming Gaussian emission profiles,

$$I(\gamma, \mu, \sigma) = \exp\left(-\frac{(\gamma - \mu)^2}{2\sigma^2}\right). \quad (2.7)$$

The inclination of the profile with respect to the surface normal,  $\mu$ , and the width of the profile,  $\sigma$ , were allowed to vary independently for cap and wall. For the 1–10 keV range, which is of interest for this project, the best fit cap profile is very narrow ( $\sigma \sim 5^\circ$ ) and has a small, but non-zero inclination ( $5^\circ < \mu < 10^\circ$ ). Their profile therefore shows the same basic features as the BS75 profile. As Fig. 2.2 shows, the BS75 profile can be approximated well with the inclined Gaussian profile from Eq. 2.7 for  $\gamma \lesssim 25^\circ$ . The wall profile found by Iwakiri et al. (2019) is isotropic ( $I(\gamma) = \text{const.}$ ) but narrows considerably above 10 keV. The maxima of cap and wall flux are found to be comparable below 10 keV.

### 2.1.4 Final choice of profiles

The standard  $1 + 2 \cos$  profile was chosen for the column wall, as it is appropriate for the more isotropic extraordinary mode (see Sect. 2.1.1). The cap profile was chosen to be an inclined Gaussian profile with  $\mu = 10^\circ$  and  $\sigma = 12^\circ$ , approximating the shape of the BS75 profile for  $\tau_0 = 10$  as shown in Fig. 2.2. BS75 reference  $\tau_0 = 20$  as an appropriate value for stopping by proton-proton collisions. However, this value gives a very narrow profile, which increases the difficulty in studying the effects of the dip at  $\vartheta = 0$  on the pulse profile. The  $\tau_0 = 10$  profile possesses a broader dip, while still showing a large anisotropy (see Fig. 2.3). The Gaussian profile was chosen over a direct use of the BS75 profile for practical reasons: the Gaussian profile is easily normalisable and its width and inclination can be independently adjusted. The effects of this approximation on the pulse profile are discussed in Sect. 3.2.

## 2.2 Additions to the LIBANS code

The following features have been added to the LIBANS code over the course of the project:

1. The BS75 profile (Eq. 2.5) have been implemented under the name `lb_int_paddles()` using the approximations for Chandrasekhar's  $H$ -function given in Eq. 2.6. The  $\tau_0$  parameter can be adjusted by resetting the qualifier `tau` (default: 10.). Note that the intensity returned by `lb_int_paddles()` is not normalised to 1.
2. The qualifier `rescale` (default: 1.) has been added to adjust the normalisation of the  $1+2\cos$ , inclined Gaussian, and BS75 emission profile functions (`lb_int_2mu()`, `lb_int_gauss()`, and `lb_int_paddles()`, respectively). Rescaling allows to manually change the relative intensities of the cap and wall profiles. The `lb_int_2mu()` function was multiplied by a factor of  $1/3$  to normalise the maximum height to 1.

# 3 Results

This chapter presents pulse profiles simulated with the LIBANS code resulting from the choice of emission profiles discussed in Sect. 2.1.4. Section 3.1 summarises the simulation setup and introduces the investigated parameters, Sect. 3.2 shows the pulse shapes arising from the emission profiles from Sect. 2.1, and Sect. 3.3–3.6 discuss the dependence of the pulse profile on the investigated parameters.

## 3.1 Simulation setup

I investigate an  $M_{\text{NS}} = 1.4 M_{\odot}$ ,  $R_{\text{NS}} = 12 \text{ km}$  neutron star with two antipodal accretion columns with radii  $r_{\text{AC}} = 1 \text{ km}$ . Cap and wall emission profiles are set as discussed in Sect. 2.1.4. The following parameters are investigated:

1. The observer inclination,  $i$ , and the inclination of the accretion columns,  $\Theta_{\text{AC1}}$  and  $\Theta_{\text{AC2}}$ , with respect to the rotational axis of the neutron star. The geometrical configuration is known to have a large impact on the emission profiles (Falkner 2012; Härer 2019).
2. The accretion column height,  $h_{\text{AC}}$ . The higher the column rises up from the surface, the more emission is expected to reach the observer from the far side of the neutron star, due to light bending (see Fig. 1.2).
3. The relative intensity of cap and wall emission. As mentioned in Sect. 1.2, this ratio can change greatly depending on the mass accretion rate and should therefore be investigated.
4. Offsets  $\Delta\Theta_{\text{AC}}$  and  $\Delta\Phi_{\text{AC}}$  in the relative polar and azimuthal positions of the accretion columns, resulting in non-antipodal configurations. Such offsets change how contributions from the individual columns add up and are therefore a good candidate to reproduce the observed asymmetric pulse shapes.

Unless otherwise noted, the investigated parameters are set to their default values:  $h_{\text{AC}} = 1 \text{ km}$ , equal normalisation of the cap and wall intensity profiles, and  $\Delta\Theta_{\text{AC}} = \Delta\Phi_{\text{AC}} = 0$  (antipodal columns). The pulse profiles have a phase resolution `nphi` = 32 and the accretion column resolution was set to `nac` = 100. Note that even though the resolutions are comparatively high, the profiles sometimes show small spikes or edges. This is purely a resolution effect, appearing either if the dip in the cap emission at  $\gamma = 0$  is visible, or in situations of strong light bending, e.g., when the accretion column is about to disappear in the shadow zone of the neutron star, because the surface area is magnified and its

### 3 Results

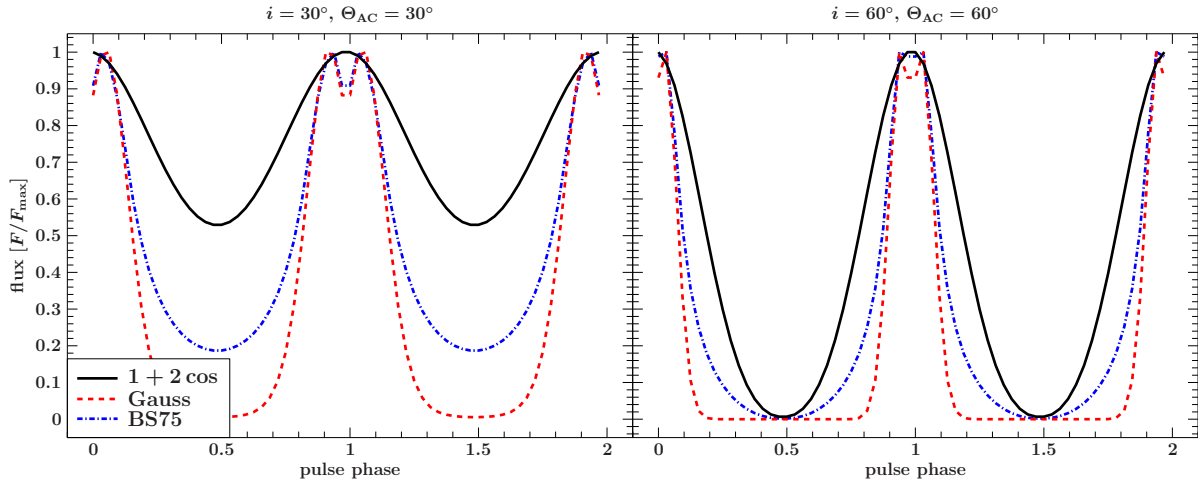


Figure 3.1: Comparison of pulse profiles resulting from the three emission profiles shown in Fig. 2.2 for a single hot spot ( $h_{ac} = 0$ ) with  $i_{ac} = i = 30^\circ$  (left) and  $i_{ac} = i = 60^\circ$  (right).

visible proportion changes rapidly. All parameters of the LIBANS simulation that are not mentioned here are left at their default values.

## 3.2 Comparison of emission profiles

Figure 3.1 shows pulse profiles from a neutron star with a single hot spot ( $h_{AC} = 0$  km) and the emission profiles from Sect. 2.1. This very simple configuration allows for a direct comparison of the pulse shapes resulting from the different emission profiles. Due to the larger anisotropy of the Gaussian and the BS75 emission profiles compared to the  $1 + 2 \cos$  profile, their fluxes depend more strongly on the pulse phase. The difference between the Gaussian and the BS75 pulse profile is largest at phase 0.5, where the emission profiles are seen under a large  $\gamma$ . The discrepancy for large  $\gamma$  is expected, as the emission profiles differ most in this case (see Fig. 2.2). Around phase 1, i.e., for small  $\gamma$ , the deviation is very small. To summarise, the flux drops of more slowly in the BS75 pulse profile than in the Gaussian profile, but their maxima are nearly identical.

At  $i = \Theta_{AC} = 30^\circ$  (left panel in Fig. 3.1), the pulse shape appears broader than at  $i = \Theta_{AC} = 60^\circ$  (right panel), because the hot spot is located closer to the rotational axis for smaller  $\Theta_{AC}$  and passes by the observer more slowly. Therefore, the angle under which the observer sees the emission profile also changes more slowly. As a result, the pulse profile broadens and the characteristic dip is visible over a larger range of phases.

### 3 Results

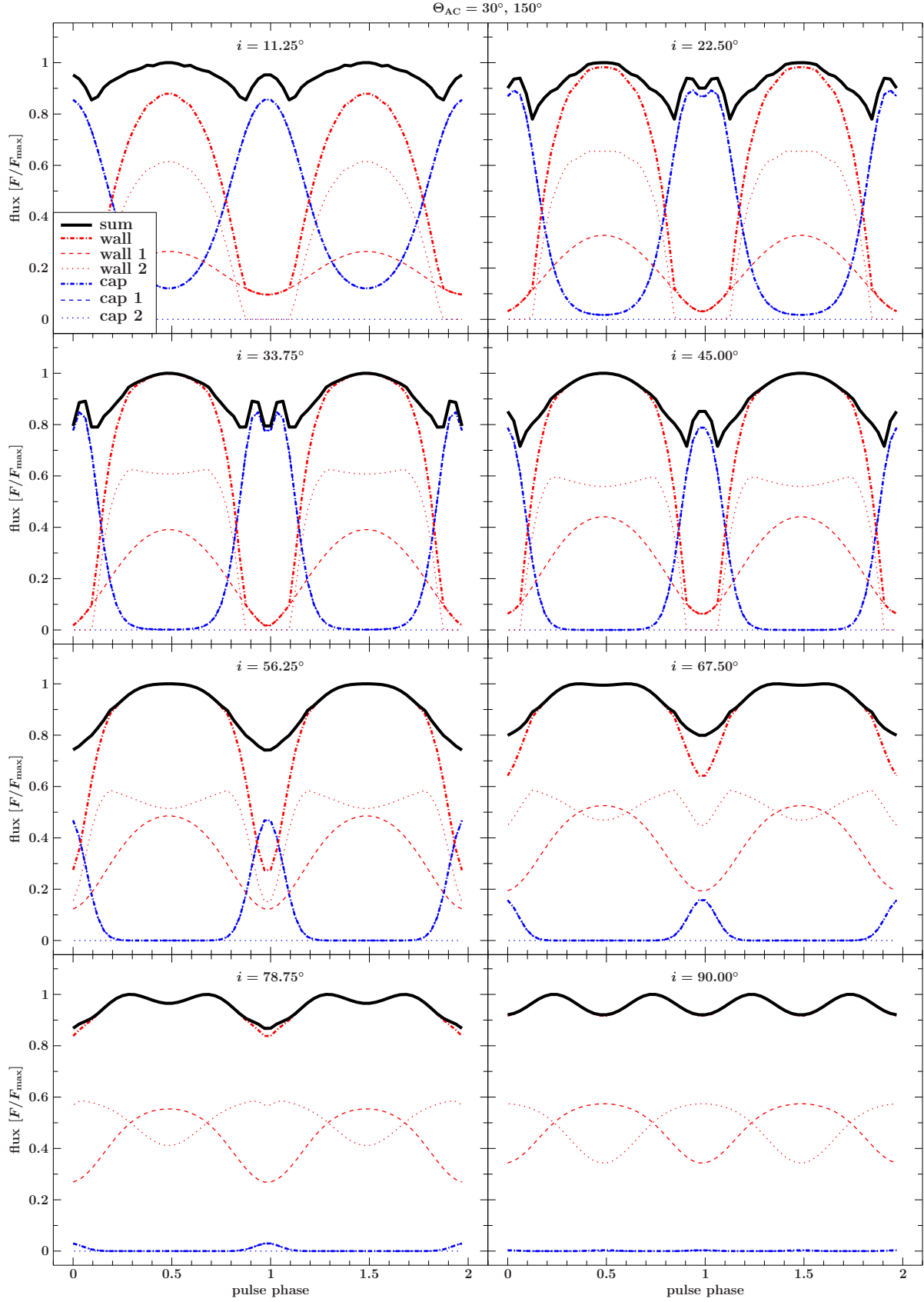


Figure 3.2: Modelled pulse profiles for  $\Theta_{AC} = 30^\circ, 150^\circ$  and varying  $i$ .

### 3 Results

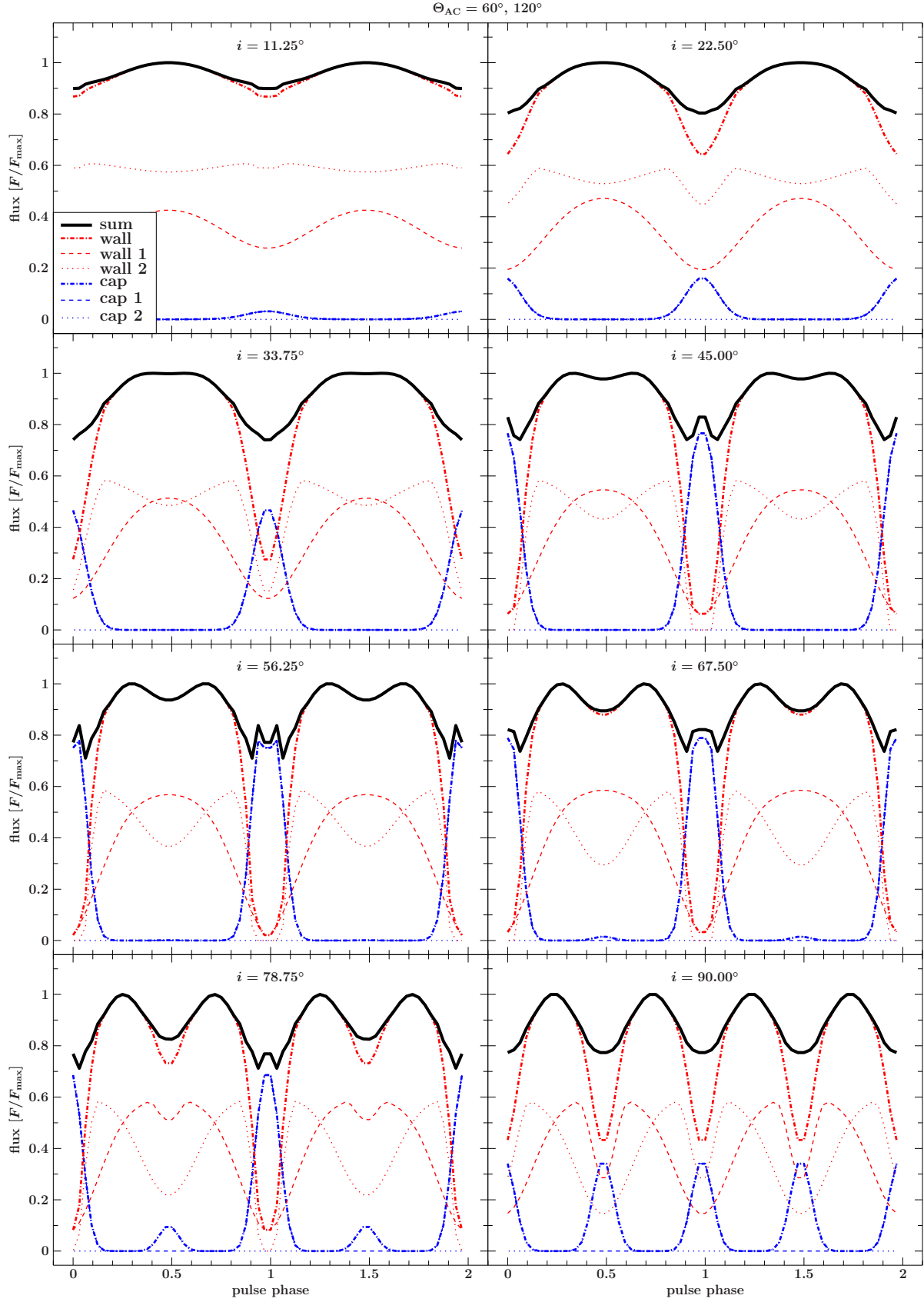


Figure 3.3: Modelled pulse profiles for  $\Theta_{AC} = 60^\circ, 120^\circ$  and varying  $i$ .

### 3.3 Observer inclination

The observer inclination,  $i$ , can greatly impact the pulse profile, including the amplitude of flux variation and the number of maxima. Figures 3.2 and 3.3 show pulse profiles for antipodal columns with  $\Theta_{AC1} = 30^\circ$ ,  $\Theta_{AC2} = 150^\circ$  and  $\Theta_{AC1} = 60^\circ$ ,  $\Theta_{AC2} = 120^\circ$ , respectively. The cap flux is strongest when the column faces the observer and the emission profile structure is most apparent for  $i \approx \Theta_{AC}$ , because only then does the observer come close to seeing the profile directly from the top, i.e., under an angle  $\gamma = 0^\circ$  (see discussion in Härer 2019).

At  $i = 90^\circ$  (last panel in Fig. 3.2 and 3.3), the emission from both columns is equal, because the observer looks face on onto the neutron star and the column are antipodal. As a result, the pulse profile has two maxima. The maxima are located at phases 0.25 and 0.75, where wall emission from both columns adds up.

Except at small  $i$ , the wall flux peaks when the column is moving behind the neutron star, because light bending enlarges the visible surface area (see also Falkner 2012). The rise in flux is broken if the column moves into the shadow of the neutron star, leading to a rapid drop (e.g., dotted line in Fig. 3.3 for  $i > 20^\circ$ ). This effect is illustrated in Fig. 3.4, which shows a model of a neutron star with an accretion column rotation away from the observer. The visible column surface area is first enlarged by light bending (middle panel), before the column disappears in the shadow zone (right panel).

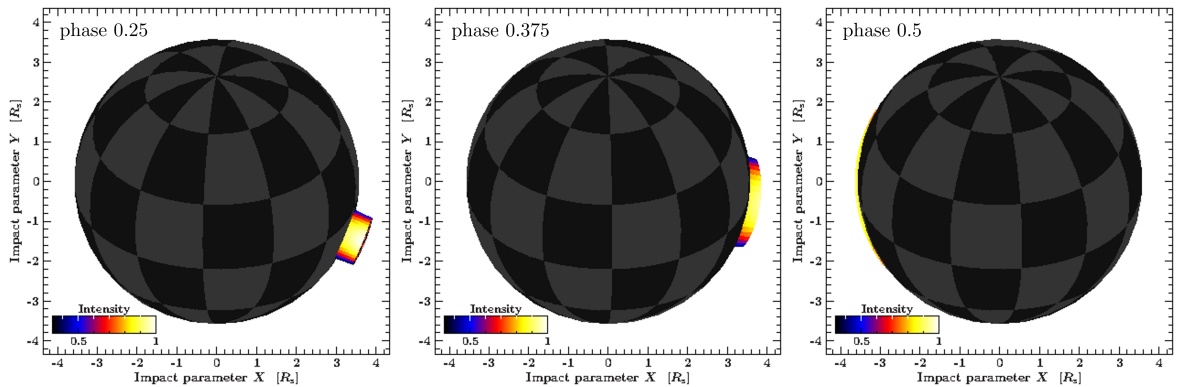


Figure 3.4: A neutron star with a single accretion column with  $\Theta_{AC} = 120^\circ$  and  $r_{AC} = h_{AC} = 2$  km, seen from  $i = 60^\circ$  at rotational phases 0.25, 0.375, and 0.5. Light bending enlarges the visible surface area of the accretion column (compare left and middle panels), shortly before it is obscured by the neutron star (right panel). Consequentially, the wall pulse profile shows an increase in flux, followed by a rapid drop (see, e.g., dotted line in Fig. 3.3 for  $i > 20^\circ$ ).

### 3.4 Accretion column height

Figure 3.5 shows pulse profiles for variable accretion column height,  $h_{AC}$ . The wall flux increases with  $h_{AC}$  relative to the cap flux. This increase is due to two factors: first, the wall surface area is larger for higher columns, which increases the total flux, because every surface element emits at the same intensity. Second, the increased height causes the accretion column to stick out of the shadow zone for longer, broadening the wall profile. In other words, at a phase where a column with a given height  $h_{AC}$  is completely obscured by the neutron star, photons emitted from  $h > h_{AC}$  can still reach the observer (see photon trajectories in Fig. 1.2), leading to a non-zero flux at this phase (compare, e.g., the wall flux in Fig. 3.5 near phase 1 for  $h_{AC} = 2000$  m and 3000 m.).

### 3.5 Relative intensity of cap and wall emission

The relative intensity of cap and wall emission is varied by adjusting their normalisation via the `rescale` qualifier introduced in Sect. 2.2. Initially, the normalisation of cap and wall emission profiles was set to 1. Figure 3.6 shows the results of rescaling the cap profile normalisation to 1/8–8 times the wall profile normalisation. As seen in the figure, the resulting flux maxima scale linearly with the normalisation factor. The result looks qualitatively similar to scaling  $h_{AC}$ , but without the broadening of the wall profile caused by light bending, which is expected as the photon trajectories are unchanged and only the intensity varies.

### 3.6 Asymmetric column configurations

All of the pulse profiles shown so far have symmetric maxima. In this section, polar and azimuthal offsets in the column positions ( $\Delta\Theta_{AC}$  and  $\Delta\Phi_{AC}$ , respectively) are introduced, to study the effect of these non-antipodal configurations on the pulse shape symmetry. The offset is always introduced to column one, which is located at the neutron star hemisphere facing the observer. Figure 3.7 shows results for  $\Delta\Theta_{AC1} = -20^\circ$  to  $20^\circ$ . The two major peaks seen for  $\Delta\Theta_{AC1} = -20^\circ$  (first panel), merge to form a single one (last panel). As there is no shift of the cap and wall maxima positions in pulse phase, the profile stays symmetric. In contrast, an offset in the azimuthal angle can result in highly asymmetric profiles, as shown in Fig. 3.8 for  $\Delta\Phi_{AC1} = 10^\circ$ – $80^\circ$ . The steep maximum comes from the fact that the flux maxima of wall two (red dotted) and cap one (blue dashed) align with increasing  $\Delta\Phi_{AC1}$ . In the antipodal configuration, they are always offset by half a pulse phase.

### 3 Results

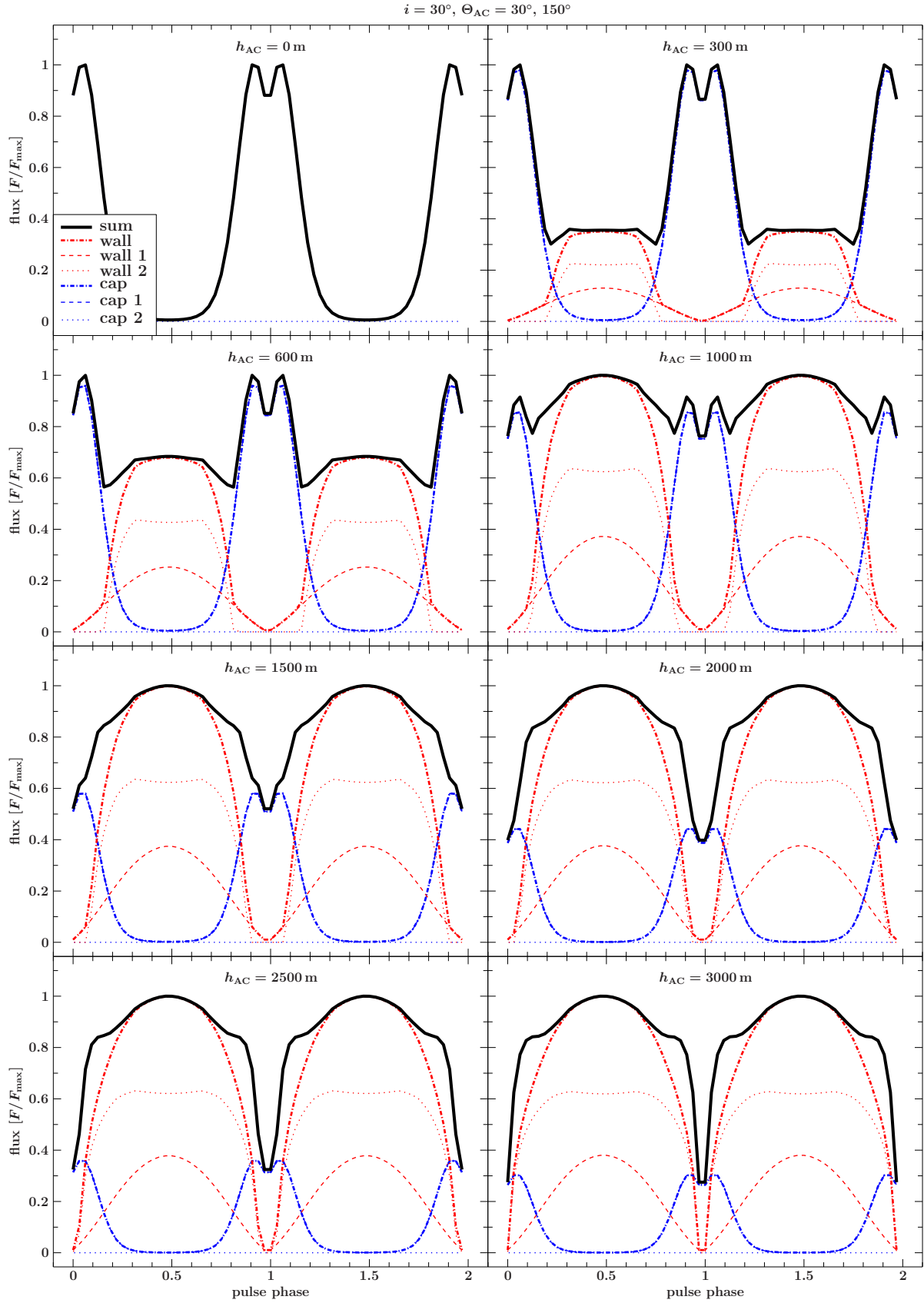


Figure 3.5: Modelled pulse profiles for variable accretion column height,  $h_{AC} = 0$ –3000 m.

### 3 Results

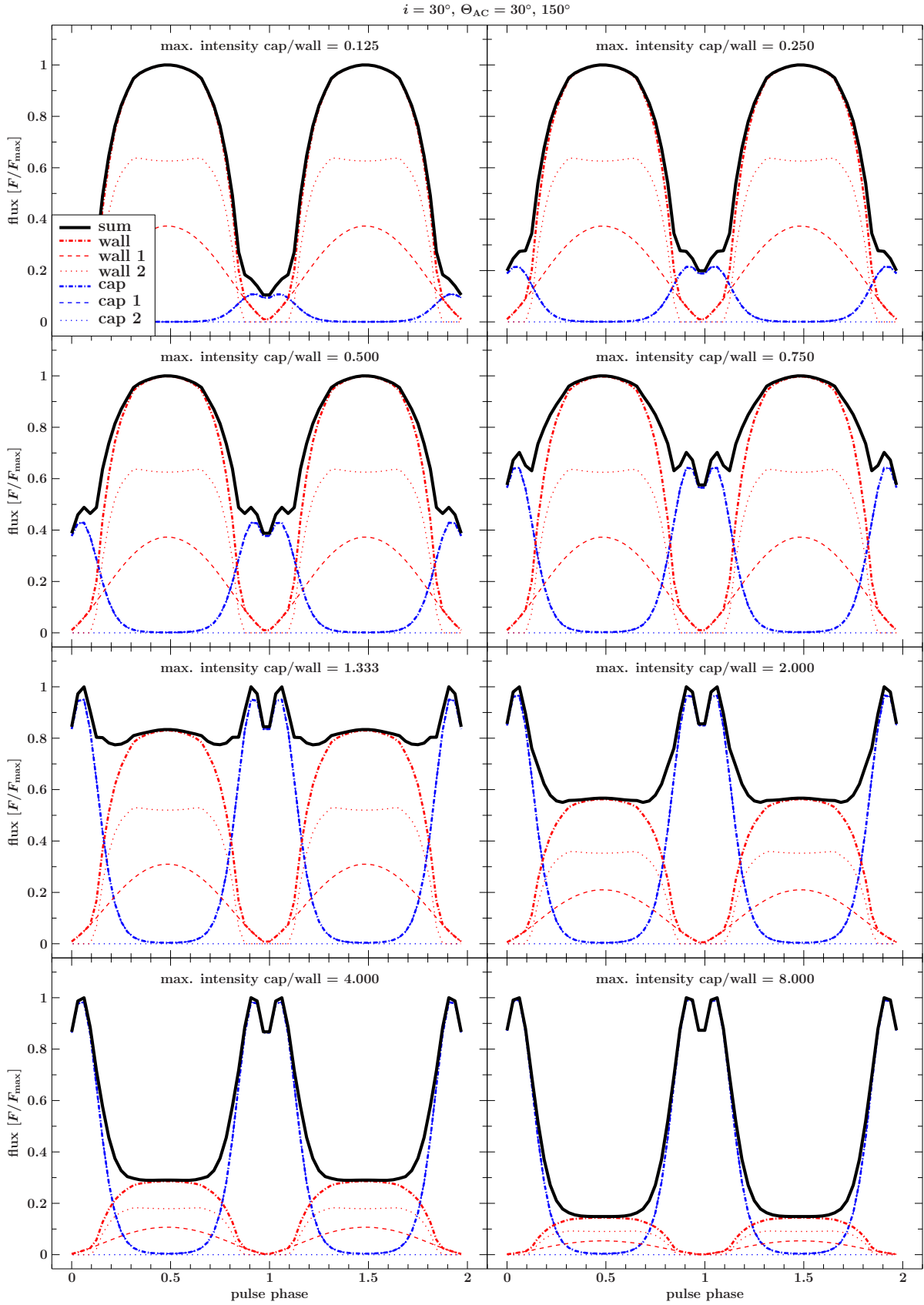


Figure 3.6: Modelled pulse profiles for variable relative intensity of cap and wall emission.



### 3 Results

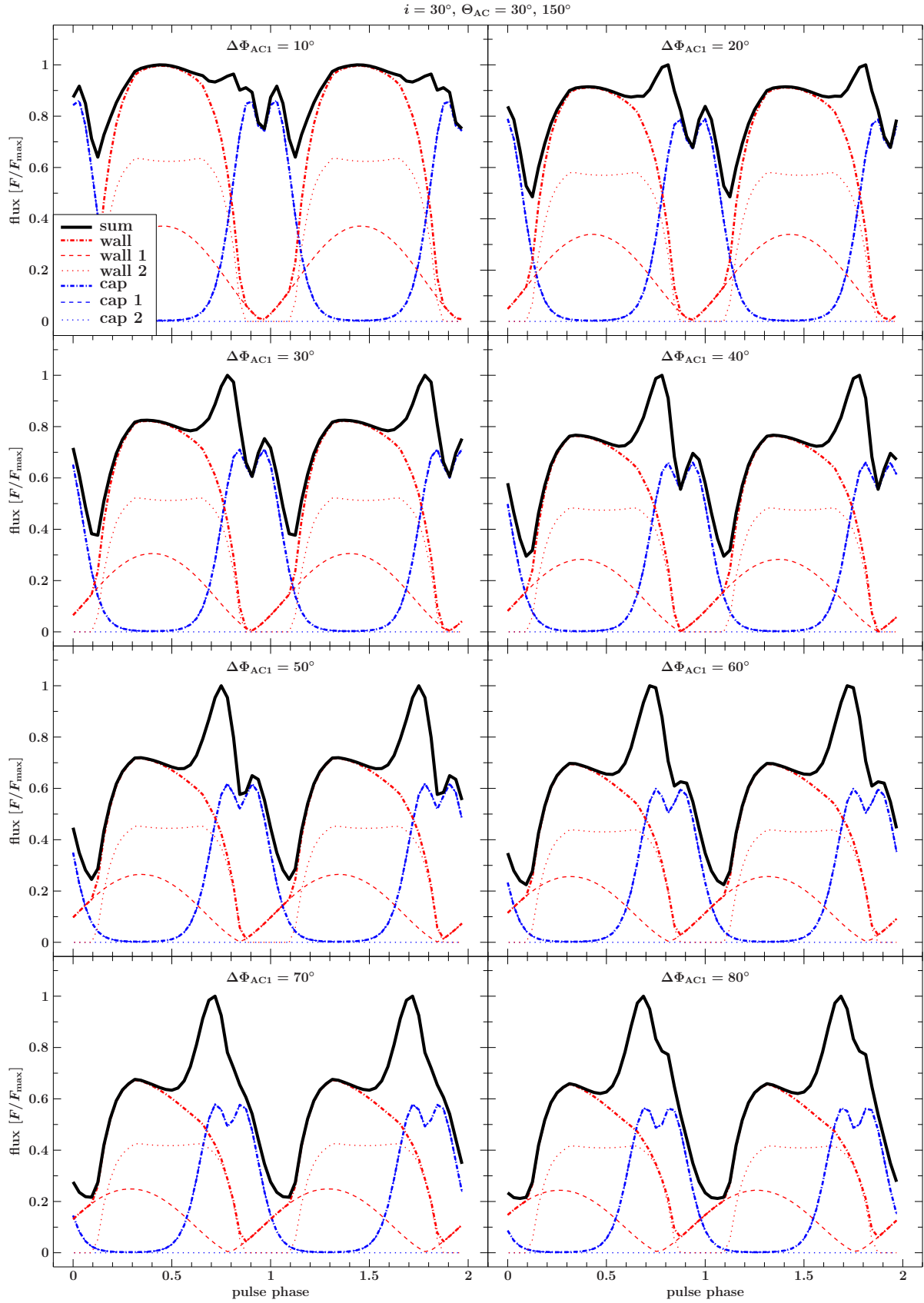


Figure 3.8: Modelled pulse profiles for an offset in the azimuthal position of the first accretion column,  $\Phi_{AC1}$ .

## 4 Summary and conclusions

I presented pulse profiles of an accreting neutron star modelled with the LIBANS code (Falkner 2012, 2018). Two different emission profiles were set for the accretion column wall and cap, the  $1 + 2 \cos$  profile and an inclined Gaussian profile, respectively. The  $1 + 2 \cos$  profile is representative of the more isotropic extraordinary polarisation mode, which predominantly escapes the column parallel to the neutron star surface. The parameters of the inclined Gaussian profile were chosen to approximate the hot spot emission profile by Basko & Sunyaev (1975) for  $\tau_0 = 10$ , which is highly focused towards small angles,  $\gamma$ , to the surface normal and shows a dip at  $\gamma = 0$ . The dependence of the pulse profiles on the observer inclination,  $i$ , the accretion column height,  $h_{AC}$ , the relative intensity of the cap and wall emission, and polar and azimuthal offsets with respect to the antipodal column configuration,  $\Delta\Theta_{AC}$  and  $\Delta\Phi_{AC}$ , was investigated. The aim was to gain a qualitative understanding of how these parameters affect the pulse profile. The main conclusions are:

1. The setup results in a variety of complex pulse profile shapes, which as much as three well-recognisable maxima per phase (Fig. 3.8,  $d\phi = -20^\circ$ ). The maxima are typically not in phase with the column on the hemisphere closest to the observer, unless the cap emission dominates, which is the case, e.g., for low column heights (see Fig. 3.5, first three panels).
2. The emission profile predicted by Basko & Sunyaev (1975) results in a narrow pulse shape. The dip is only observable if  $i \approx \Theta_{AC}$  and if the phase resolution is high enough. For  $\tau_0 > 10$ , as referenced in Basko & Sunyaev (1975), the pulse shape would narrow further, making the dip increasingly difficult to observe.
3. Asymmetric profiles are only seen for an azimuthal offset,  $\Delta\Phi_{AC}$ , within the investigated parameter ranges. The narrow cap emission profile makes the pulse profile particularly sensitive to  $\Delta\Phi_{AC}$ . An offset of  $\Delta\Phi_{AC1} = 30^\circ$  caused a  $>20\%$  asymmetry in the flux maximum (see Fig. 3.8, third panel). Given these results, azimuthal offsets appear to be a likely origin of the asymmetries in observed pulse profiles.

Pulse profile modelling reveals how the cap and wall flux adds up to form the overall pulse profile. This information is not only helpful to understand the parameter dependences of pulse shapes, but might also be useful to verify models with polarimetry, as different polarisation modes are expected to dominate the cap and wall emission. X-ray polarimetry missions such as *IXPE* (Weisskopf et al. 2016) will hopefully bring us a step closer to understanding the origin of pulse profiles.

# Bibliography

- Basko, M. M. & Sunyaev, R. A. 1975, *A&A*, 42, 311
- Becker, P. A., Klochkov, D., Schönherr, G., et al. 2012, *A&A*, 544, A123
- Becker, P. A. & Wolff, M. T. 2007, *APJ*, 654, 435
- Beloborodov, A. M. 2002, *APJ Letters*, 566, L85
- Bildsten, L., Chakrabarty, D., Chiu, J., et al. 1997, *APJ Supplement Series*, 113, 367
- Caballero, I. & Wilms, J. 2012, *Memorie della Societa Astronomica Italiana*, 83, 230
- Canuto, V., Lodenguai, J., & Ruderman, M. 1971, *Physical Review D*, 3, 2303
- Falkner, S. 2012, Master's thesis, FAU Erlangen-Nürnberg
- Falkner, S. 2018, PhD thesis, FAU Erlangen-Nürnberg
- Giacconi, R., Gursky, H., Kellogg, E., Schreier, E., & Tananbaum, H. 1971, *APJ Letters*, 167, L67
- Hapke, B. 2002, *Icarus*, 157, 523
- Härer, L. 2019, Bachelor's Thesis, FAU Erlangen-Nürnberg
- Iwakiri, W. B., Pottschmidt, K., Falkner, S., et al. 2019, *APJ*, 878, 121
- Lai, D. 2001, *Reviews of Modern Physics*, 73, 629
- Lamb, F. K., Pethick, C. J., & Pines, D. 1973, *APJ*, 184, 271
- Lattimer, J. M. 2012, *Annual Review of Nuclear and Particle Science*, 62, 485
- Lyubarskii, Y. É. 1986, *Astrophysics*, 25, 577
- Postnov, K. A., Gornostaev, M. I., Klochkov, D., et al. 2015, *MNRAS*, 452, 1601
- Schwarm, F. W., Schönherr, G., Falkner, S., et al. 2017, *A&A*, 597, A3
- Sokolova-Lapa, E., Gornostaev, M., Wilms, J., et al. 2021, *A&A*, 651, A12
- Staubert, R., Trümper, J., Kendziorra, E., et al. 2019, *A&A*, 622, A61

## *Bibliography*

Tananbaum, H., Gursky, H., Kellogg, E. M., et al. 1972, APJ Letters, 174, L143

Weisskopf, M. C., Ramsey, B., O'Dell, S., et al. 2016, in Society of Photo-Optical Instrumentation Engineers (SPIE) Conference Series, Vol. 9905, Space Telescopes and Instrumentation 2016: Ultraviolet to Gamma Ray, ed. J.-W. A. den Herder, T. Takahashi, & M. Bautz, 990517